Aerothermal Prediction of Hypersonic Re-entry Configurations: Effects of Geometry, Altitude, and Chemical Kinetics

Rachid Renane *, Rachid Allouche, Ahmed Neche, and Oumaima Zmit

Institute of Aeronautics and Space Studies Aeronautical Science Laboratory (LSA), University of Blida1, Blida, Algeria
Email: r.renane-aerospatiale@univ-blida.dz (R.R); racalloche@gmail.com (R.A); ahm.nach9@gmail.com (A.N.); oumzemit@gmail.com (O.Z)
*Corresponding author

***Abstract*—Accurate prediction of aerothermal loads under hypersonic thermochemical nonequilibrium conditions is critical for the design of future atmospheric re-entry vehicles. This study presents a comprehensive numerical investigation of the aerodynamic and aerothermal performance of three representative re-entry configurations (a lifting delta wing, a cone-flare body, and a blunt-spiked nose) under realistic hypersonic flight conditions. The compressible Navier–Stokes equations are solved using ANSYS Fluent, incorporating detailed thermochemical nonequilibrium effects through Park's five-species, 17-reaction air model. Results are systematically compared with perfect-gas and reduced-reaction models to quantify the impact of dissociation on heating predictions. Parametric analyses are conducted over Mach numbers 15–25, altitudes 60–76 km, and angles of attack up to 40°, focusing on lift-to-drag ratio, aerodynamic braking, wall temperature, and heat flux distribution. Adaptive mesh refinement ensures accurate resolution of shock–boundary-layer interactions while maintaining computational efficiency. The results demonstrate that lifting configurations significantly enhance controllability, with the delta wing achieving up to a 63% improvement in lift-to-drag ratio compared to the cone-flare. Detailed chemistry reduces peak post-shock temperatures by approximately 28% relative to perfect-gas assumptions due to endothermic dissociation. Furthermore, the blunt-spiked nose effectively mitigates stagnation heating, reducing nose temperature by about 12.5% through bow-shock displacement. Numerical predictions show good agreement with available experimental schlieren and heat-transfer data. Overall, the study highlights the synergistic role of geometry, flight parameters, and chemical kinetics in optimizing aerothermal performance, providing validated guidelines for the development of next-generation lifting hypersonic re-entry vehicles.**

***Keywords*—hypersonic reactive flows, aerodynamic heating, dissociation phenomena, lifting re-entry, hypersonic vehicle configurations, and shock-wave interactions**

I. Introduction

During preliminary atmospheric re-entry vehicles design, systematic variations in geometry, trajectory, and flight conditions are essential for evaluating their impact on aerodynamic performance, thermal protection, and overall mission safety. A successful re-entry requires the vehicle to withstand extreme aerodynamic heating and deceleration while maintaining sufficient control authority to ensure precise and reliable landing performance [1, 2]. Consequently, the accurate prediction of aerothermodynamic loads under hypersonic flow conditions remains a cornerstone of modern aerospace engineering. At Mach numbers between 15 and 25, hypersonic flows are dominated by molecular dissociation, vibrational excitation, and strong shock interactions, which substantially influence stagnation temperature and surface heat flux [3, 4]. Combined with viscous skin-friction heating, these mechanisms can elevate surface temperatures beyond the limits of conventional structural materials, motivating advanced Thermal Protection Systems (TPS) and robust predictive methodologies [5–7]. Ionization and radiation effects remain secondary below velocities of approximately 6000–8000 m/s, while chemical dissociation dominates the thermal response within this range [1, 8, 9]. Vehicle geometry and angle of attack are equally decisive parameters in hypersonic aerothermodynamics. High Lift-to-Drag (L/D) ratios enable controlled aerodynamic braking, allowing gradual dissipation of kinetic energy and improved landing accuracy. Numerous studies have demonstrated that lifting configurations can outperform Shuttle-type designs by generating higher lift coefficients while simultaneously reducing thermal loads [10–14]. Delta-wing geometries, in particular, enhance lift through strong compression shocks on the windward surface, but are also prone to intense shock–boundary layer interactions that strongly influence heat transfer and boundary-layer transition [12, 15–19]. Recent high-fidelity experimental and numerical studies

Manuscript received April 17, 2026; revised June 10, 2026; accepted July 20, 2026; published September 8, 2026.

doi: 10.18178/ijmerr.15.5.458-473

further highlight the dominant role of geometry in hypersonic flows. In particular, Seltner *et al.* [20] investigated the transition from laminar to turbulent flow over a Mach 6.5 delta-wing configuration by combining wind-tunnel measurements with numerical simulations, Identifying shock-induced instabilities and secondary modes as key drivers of transition and heat-flux amplification [21]. High-resolution numerical simulations have demonstrated that attachment-line boundary layers over blunt swept bodies are highly sensitive to surface roughness, which can trigger subcritical transition and significantly intensify heat transfer [21]. These findings emphasize the necessity of advanced turbulence modeling, fine grid resolution, and adaptive numerical strategies for accurate aerothermal prediction [22]. Blunt-body geometries, widely used to reduce stagnation-point heating, exhibit complex shock interactions. Experiments on multiple free-flying blunt bodies in hypersonic flow [23] reveal strong shock–shock and shock–wake interactions that significantly alter pressure distribution, aerodynamic forces, and vehicle stability. Further studies on nose-tip bluntness [24] demonstrate that greater bluntness delays boundary-layer transition and decreases peak heat flux by weakening the detached bow shock. The findings highlight the critical role of geometric optimization in thermal protection strategies, such as blunt-nose and aerospike configurations [10, 14].

Foundational contributions further clarify the underlying mechanisms. A thin-shock-layer formulation was introduced to improve shock and pressure prediction for delta-wing flows [19]. Computational Fluid Dynamics (CFD) analyses have been employed to study hypersonic vehicle wakes, and turbulent cavity-heating correlations have been refined with quantified uncertainties [25]. Concave undersurfaces have been shown to reduce heating while improving L/D performance across Mach numbers from 6 to 22 [12]. Direct numerical simulations indicate that compression-ramp flows lead to sharp amplification of wall heat flux [5], and adaptive mesh refinement effectively captures hypersonic flow features in close agreement with experimental data [26].

Building on these insights, the present study investigates the aerothermal behavior of three representative configurations—a delta wing, a cone-flare geometry, and a blunt nose equipped with an aerospike under hypersonic thermochemical non-equilibrium flow. Simulations are performed for altitudes of 60.96–76.20 km, velocities of 4.88–7.32 km/s, and angles of attack from 0° to 40°. Air is modeled as a five-species mixture (O_2, N_2, NO, O, and N) using Park's 17-reaction chemical-kinetic scheme. Adaptive mesh refinement ensures accurate prediction of shock–boundary layer interactions. Results quantify the combined influence of geometry, flight conditions, and chemical kinetics on surface heat flux, lift-to-drag ratio, and aerodynamic braking efficiency, and are validated against experimental schlieren, heat-transfer data, and recent high-fidelity studies [10, 14, 22, 27, 28], providing a comprehensive assessment of design strategies for future lifting re-entry vehicles.

Unlike previous studies that focus separately on either vehicle geometry, chemical kinetics, or thermal protection strategies, the present work provides a unified aerothermal assessment of three representative hypersonic re-entry configurations under identical flight conditions. The novelty of this study lies in: (i) the simultaneous comparison of lifting and non-lifting re-entry geometries, (ii) the coupling of detailed thermochemical nonequilibrium chemistry with aerodynamic performance evaluation, (iii) the quantification of altitude and angle-of-attack effects on both heating and controllability, and (iv) the assessment of blunt-spike thermal mitigation within the same computational framework. These contributions provide practical design guidelines for future hypersonic re-entry vehicles.

II. NEMERICAL METHODOLOGY

A. Geometry and Mesh Setup

To comprehensively evaluate aerothermal prediction strategies for lifting re-entry vehicles, three representative geometries were investigated: a delta wing, a cone-flare body, and a blunt-spiked nose. These models were carefully selected to represent different physical regimes of hypersonic re-entry, ranging from controlled lifting configurations to strongly hypersonic bodies and thermal mitigation designs.

1) Delta wing configuration

The delta wing (Fig. 1) is derived from a shuttle-like lifting configuration, characterized by a sweep angle of 15°, and provides a reference for assessing lift-to-drag optimization under hypersonic conditions [29, 30]. Its streamlined shape makes it an ideal configuration for evaluating aerodynamic braking and controlled descent trajectories. The delta body mesh is shown in Fig. 2, while mesh quality indicators, including skewness and non-orthogonality, were carefully generated, evaluated, and verified to comply with ANSYS Fluent best-practice guidelines, thereby ensuring numerical robustness, stable convergence, and physical fidelity of the simulations.

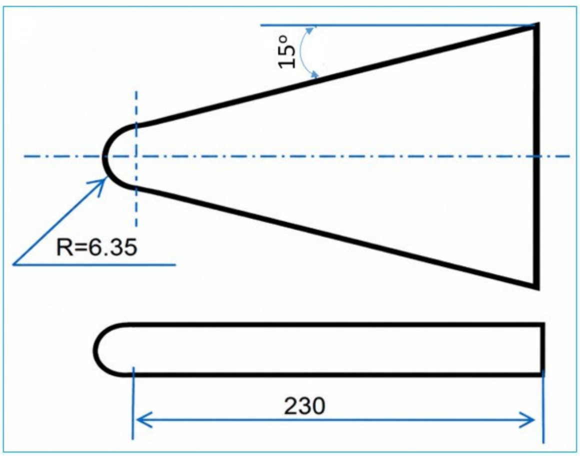

Fig. 1. Delta geometry creation.

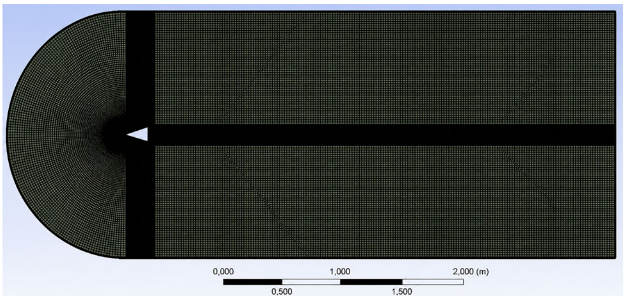

Fig. 2. Delta body mesh.

2) Cone-flare configuration

The cone-flare geometry (Fig. 3) represents a re-entry configuration, where axial compression and strong shock–boundary layer interactions dominate. This shape is crucial for investigating heat-flux amplification in separated flows.

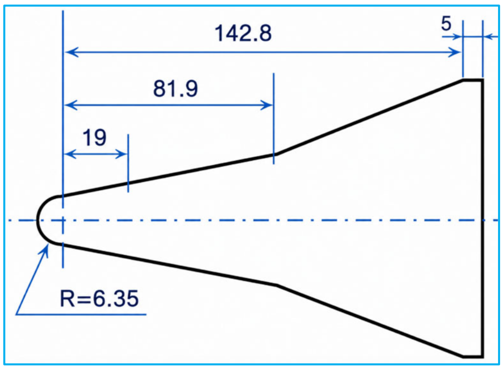

Fig. 3. Cone flare body geometry.

A hybrid meshing approach was applied: most of the computational domain was meshed with unstructured triangular elements, while a structured near-wall mesh was employed to resolve viscous layers. Edge sizing and inflation were used to adequately capture wall heat flux and shock–surface interactions. The cone-flare mesh is shown in Fig. 4. Mesh quality analysis confirmed that skewness and non-orthogonality satisfied ANSYS quality criteria, ensuring robust flow predictions under steep gradients.

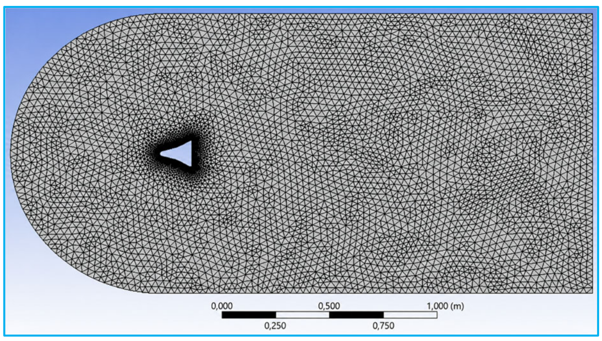

Fig. 4. Cone flare body mesh.

3) Blunt-spiked nose configuration

The blunt-spiked nose (Fig. 5), based on the Lobb sphere concept, is designed to reduce stagnation-point heating by shifting the bow shock upstream [30]. The spike geometry is defined with d/D = 1/10 and L/D = 9/10 for the spike-to-sphere diameter and spike length-to-diameter ratios, respectively (see Table I). These geometric ratios are consistent with previous studies, which have demonstrated their effectiveness in mitigating stagnation heat flux during hypersonic atmospheric re-entry.

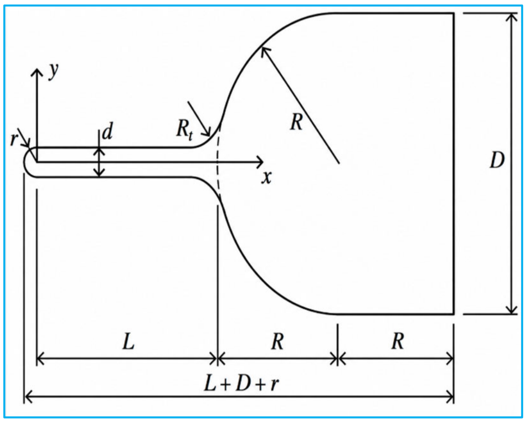

Fig. 5. Blunt spike geometry.

TABLE I. BLUNT SPIKE DIMENSIONS

Parameter	Value (mm)
D	12.7
d	1.27
L	11.43
r	0.635
R	6.35
Rt	2.5

The blunt-spike mesh is shown in Fig. 6, with its structured grid clearly visible. Mesh quality criteria, including skewness and non-orthogonality, were verified and satisfied ANSYS accepted limits.

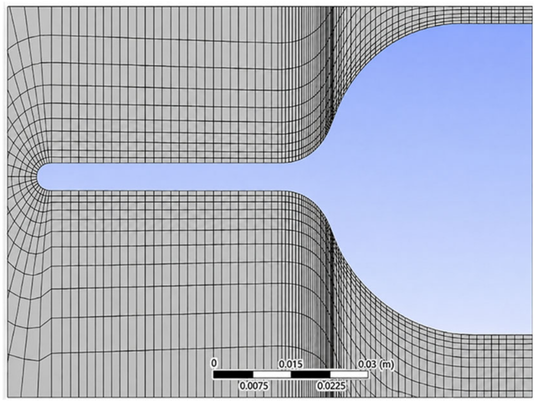

Fig. 6. Blunt spike mesh.

4) Computational domain and boundary conditions

The computational domain was designed following the guidelines presented in [30] to minimize boundary interference while maintaining computational efficiency. The vertical and lateral boundaries were set to 5L (with L = 0.23 m, reference length), The computational domain extended 5H upstream and 15H downstream of the body, with H corresponding to the characteristic height of the configuration.

The wall was treated as a no-slip, adiabatic surface, and the surrounding domain as a pressure far-field. This configuration allowed accurate resolution of shock standoff distances and thermal boundary layers without introducing spurious reflections.

5) Free-stream conditions

The free-stream boundary conditions used in the present simulations are summarized in Table II, which reports the thermochemical parameters corresponding to a 17-reaction mechanism. These data, adapted from [31, 32], define the inflow properties—angle of attack, Mach number, reaction number, free-stream temperature, density, and static pressure—used in the subsequent analysis of chemical nonequilibrium effects (see Section "Influence of Chemical Reaction Models").

TABLE II. FREE-STREAM BOUNDARY CONDITIONS

α	**Mach number**	**Reaction number**	**T_∞ [k]**	**ρ_∞(kg/m^3)**	**P_∞ [Pa]**
0°	15.35	17	293	$7.896 \cdot 10^{-3}$	664

Table III extends the baseline conditions by presenting altitude-dependent free-stream parameters representative of a conventional atmospheric re-entry flight path. The data, in agreement with Lordi *et al.* [33], describe the variation of static pressure, temperature, and density with altitude, representing the external flow environment during the Shuttle's high-enthalpy descent.

TABLE III. ALTITUDE-DEPENDENT FREE-STREAM CONDITIONS

Altitude [Km]	**Mach**	**P_∞ [Pa]**	**ρ_∞ [Kg/m^3]**	**T_∞ [K]**
60.96	15.562	19.259	$2.745\ 10^{-4}$	244.4
67.06	20.154	8.102	$1.239\ 10^{-4}$	227.6
76.20	25.420	1.968	$3.327\ 10^{-5}$	206.1

These free-stream conditions encompass the most critical phases of atmospheric re-entry, where dissociation-driven heating dominates the thermal environment, while ionization and radiative phenomena remain secondary [1, 9, 22]. The adopted parameters ensure that the simulations accurately reproduce the high-enthalpy regime characteristic of hypersonic flows, thereby reinforcing the physical relevance of the results for Thermal Protection System (TPS) design and aerothermal performance optimization.

6) Comparative synthesis of the three re-entry configurations

Table IV summarizes the main geometric parameters, meshing strategies, and physical roles of each configuration, offering a concise overview of their specific contributions to aerothermal prediction and mitigation in hypersonic re-entry.

TABLE IV. COMPARATIVE SYNTHESIS OF GEOMETRIES

Aspect	**Delta Wing (Figs. 1, 2)**	**Cone-Flare (Figs. 3, 4)**	**Blunt-Spiked Nose (Figs. 5, 6)**
Key Characteristics	Sweep angle 15°; Shuttle-like lifting body [29].	Classical re-entry configuration [30, 34].	Nose-mounted spike, d/D = 1/10 and L/D =9/10 [5, 6, 23]
Mesh Strategy	Structured + local refinement (Fig. 2)	Hybrid mesh: unstructured bulk + structured near-wall (Fig. 4)	Structured mesh+ local refinement (Fig. 6)
Physical Role	High L/D; strong compression shocks; controlled braking	Strong shock–boundary layer interactions; high heating	Weakens bow shock; redistributes stagnation heat
Relevance to Study	Baseline for lifting re-entry; reference for L/D optimisation	Represents hypersonic re-entry; critical case for thermal protection system	Demonstrates mitigation strategy for nose heating

B. Numerical Methodology: Grid Independence and Physical Models

To verify numerical reliability, mesh sensitivity was evaluated before performing the aerothermal calculations. Several mesh densities were evaluated, with particular emphasis on the near-wall region, as precise resolution of wall heat transfer is essential for assessing thermal protection performance under hypersonic re-entry conditions.

The wall-adjacent region was discretized using a gradient-based structured mesh, enabling localized refinement in zones exhibiting steep gradients of temperature, pressure, and velocity. This strategy prevented unnecessary refinement in uniform flow regions and focused computational resources on areas dominated by shock–boundary layer interactions and strong dissociation phenomena. Progressive grid refinement led to converged solutions with diminishing sensitivity to mesh resolution.

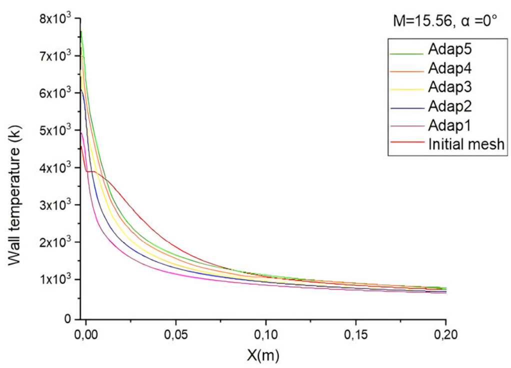

Fig. 7. Delta wing body grid independency.

To balance numerical accuracy and computational efficiency, grid Adapt 4 was retained for the delta-wing body (Fig. 7), while grid Adapt 3 was used for the cone-flare (Fig. 8) and blunt-spike (Fig. 9) configurations. This selection provided stable and consistent results without excessive computational cost. Mesh sensitivity analysis confirmed the adequacy of the grids, with adaptive refinement continued until further enrichment caused negligible changes in key thermal indicators, such as wall and relaxation-zone temperatures, demonstrating mesh independence.

The final optimal meshes were defined as follows: Adapt 4 for the delta-wing body (129,963 cells; 13,010 nodes), Adapt 3 for the cone-flare body (575,384 cells; 30,069 nodes), and Adapt 3 for the blunt-spikebody (572,744 cells; 378,518 nodes).

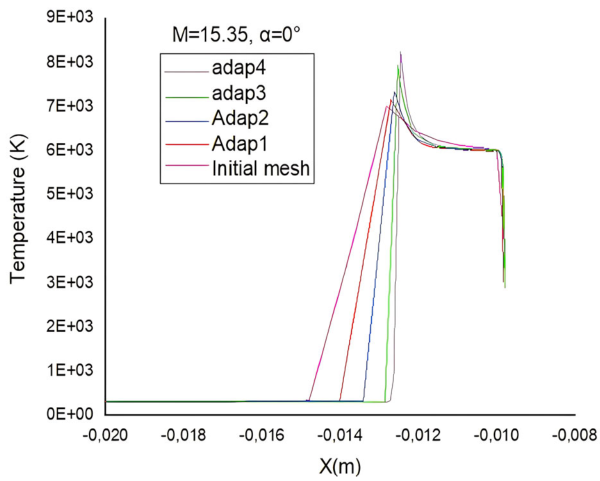

Fig. 8. Cone-flare body grid independency.

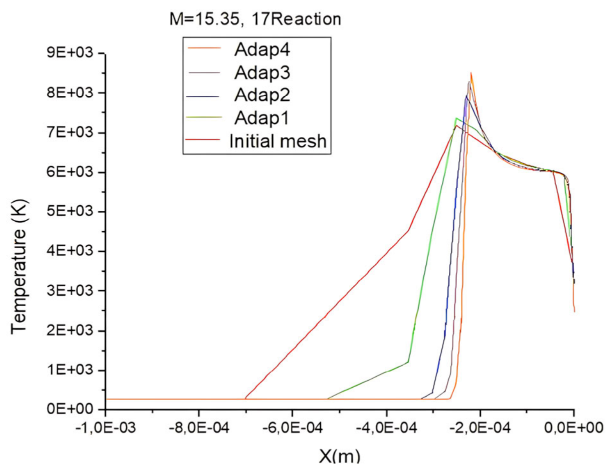

Fig. 9. Blunt spike grid independency.

Since this study focuses on hypersonic thermochemical non-equilibrium flows, simulations were performed using the steady density-based solver in ANSYS Fluent within a RANS (Reynolds-Averaged Navier–Stokes) framework, ensuring accurate prediction of high-temperature effects (see Appendix A). This formulation was chosen because it reduces the overall mesh size and computational time while preserving the fidelity of the shock–layer and boundary-layer resolution. Such efficiency is essential when coupling complex chemical reaction mechanisms with multi-geometry comparisons.

For turbulence modelling, the *k-ω* SST (Shear Stress Transport) model was employed. This hybrid formulation merges the advantages of the *k-ε* model in the free stream with the *k-ω* model in near-wall regions, allowing robust predictions of shock-induced separation and boundary-layer development. The *k-ω* SST model is particularly well suited for hypersonic applications, as it captures thin viscous boundary layers, where molecular viscosity dominates and turbulence is strongly damped, while still providing reliable transition and separation behavior.

Chemical non-equilibrium effects were incorporated by solving the species transport and reaction equations, which account for convection, diffusion, and source terms of multiple reacting species (See Appendix A). Air was modeled as a five-species mixture (O_2, N_2, NO, O, N) using Park's 17-reaction mechanism (see Table V). Additional information on the chemical kinetic model is provided in Appendix A.

This approach enables an accurate representation of dissociation phenomena that dominate the thermal environment between Mach 15 and 25.

To minimize numerical diffusion and enhance the accuracy of species transport, gradients of solution variables were computed using the Least-Squares Cell-Based method. This approach was selected because it provides second-order accuracy in gradient reconstruction, reduces spurious diffusion, and remains computationally efficient. Its adoption ensures more reliable predictions of temperature distributions, heat fluxes, and shock–boundary layer interactions, all of which are critical for evaluating aerothermal protection strategies in re-entry vehicles.

TABLE V. QUANTITATIVE AND QUALITATIVE VALIDATION RESULTS

Parameter	Configuration	Present Study	Literature value	Reference	Relative diference(%)
Peak wall streamline temperature	Delta wing Fig. 10	4600 K	4540 K	Lordi *et al.* [33]	1.3 %
Peak Wall Temperature (Outer Streamline)	Delta wing Fig. 11	5000 K	5100 K	Lordi *et al.* [33]	1.9 %
Shock structure and bow-shock position	Blunt body Fig. 13, 14	Good agreement	Experimental schlieren	Schrijer *et al.* [29]	Qualitative validation
Flow field wave structure	spiked blunt body (Fig. 22)	Good agreement	Experimental Schlieren photograph	Guzmán-Bohórquez *et al.* [28]	Qualitative validation

C. Validation of Thermochemical Flow Predictions

The computational results of high-enthalpy thermochemical flows over the studied configurations are presented in this section. For validation purposes, simulations were first performed on a representative Shuttle-like delta wing at a 20° angle of attack, under conditions consistent with hypersonic re-entry.

Fig. 10 shows the temperature variation along the body surface streamline and wall temperature along the external streamline, compared with numerical results in [33] that incorporate detailed modeling of ionization phenomena in hypersonic flows. The comparison shows a generally good agreement between our CFD predictions and Lordi's reference data, confirming that the implemented chemical non-equilibrium model is capable of capturing the dominant physical mechanisms.

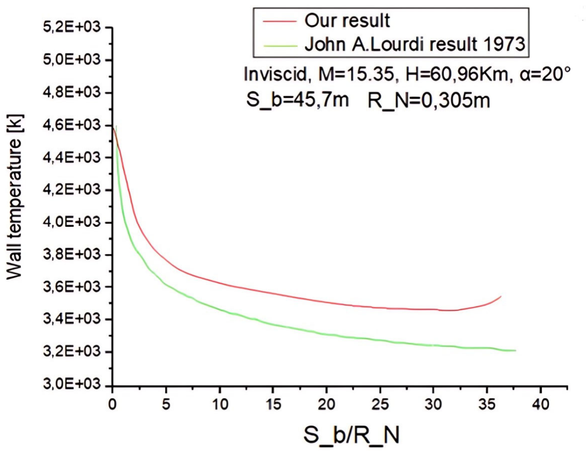

(a)

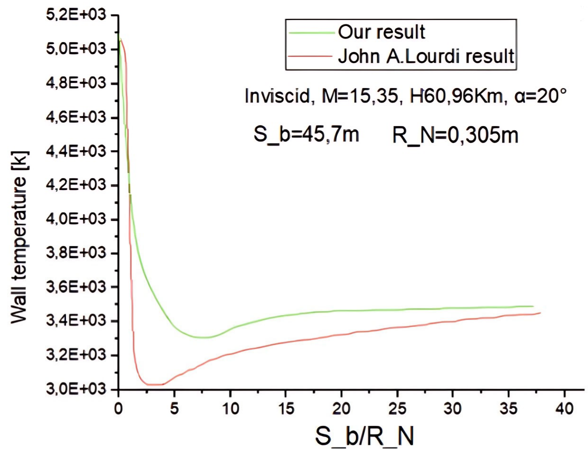

(b)

Fig. 10. Temperature filed along (a) streamline $\alpha = 20°$; (b) outer-streamline $\alpha = 20°$.

However, in localized regions where the flow temperature peaks, particularly in the shock–layer stagnation zone, the maximum discrepancy reaches about 10%. This deviation is attributed to the endothermic ionization phenomenon, explicitly considered in [1, 7, 33], but neglected in the present work, consistent with the modeling assumption that ionization effects become significant only above approximately 6000 m/s. As the flow cools downstream of the nose, dissociation remains the dominant mechanism, and agreement improves, with errors reduced to below 5% over most of the surface.

This trend is consistent with earlier investigations [1, 7], which documented the transition from ionization-dominated to dissociation-driven regimes. The shock shape and streamline patterns near the nose are shown in (Fig. 11).

The simulations capture the characteristic detached bow shock of hypersonic blunt-body flows, with well-resolved compression layers and boundary-layer interactions. These findings confirm that the adopted mesh refinement and chemical-kinetics model provide sufficient fidelity to resolve both global shock topology and local surface thermal loads.

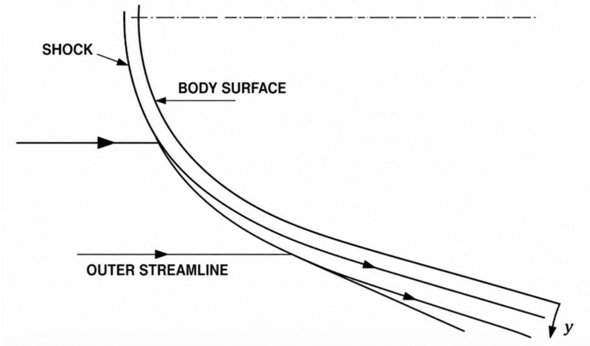

Fig. 11. Shock shape and streamline pattern in nose region [33].

D. Validation Against Schlieren Data

The reliability of the numerical model was further evaluated by comparing the lifting delta-wing configuration with a hypersonic cone-flare body under identical flow conditions. Experimental schlieren images from previous studies [29, 30, 34] are shown in Fig. 12, while Fig. 13 presents the corresponding CFD results obtained in this work.

The simulations accurately reproduce the bow-shock position, curvature, and overall flow topology observed experimentally. In particular, the detached bow shock formed upstream of the cone-flare and the compression shocks along the delta-wing undersurface are captured with high fidelity. This level of agreement confirms that the adopted mesh refinement and turbulence–chemistry interaction modeling are sufficient to resolve shock–boundary-layer dynamics in chemically reacting hypersonic flows. Such validation strengthens confidence in applying the present methodology to more complex configurations, including aerothermal mitigation concepts such as the blunt-spike geometry.

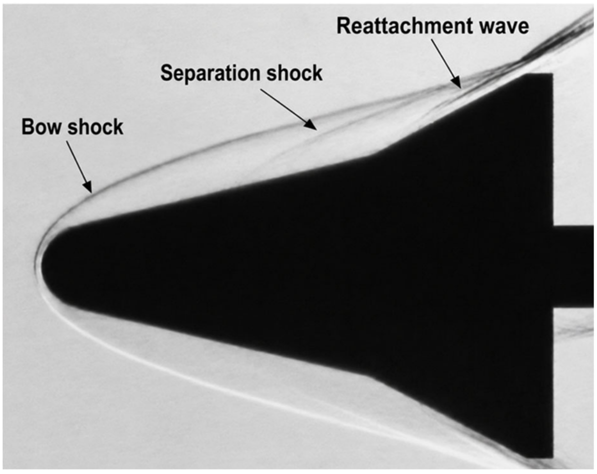

Fig. 12. Experimental shock structure around a blunt body.

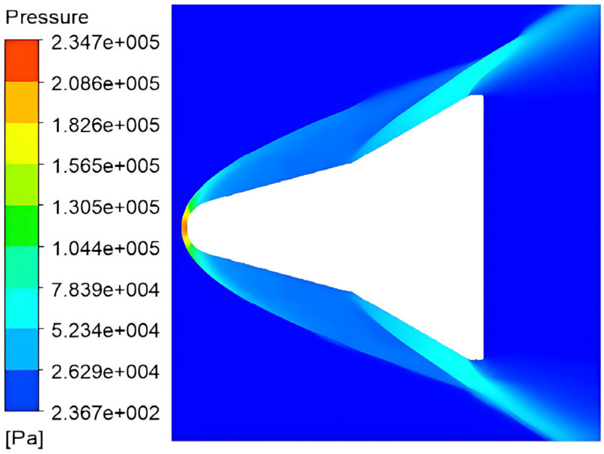

Fig. 13. Pressure contours around a hypersonic blunt body.

III. Results and Discussion

A. Effects of Vehicle Shape on Aerodynamic Braking

A direct comparison between the lifting delta wing and the cone-flare during atmospheric entry at Mach number M = 15.56 and Altitude H = 60.96 km highlights the critical role of geometry in aerodynamic braking and trajectory control (Fig. 14(a) and (b)). At low angles of attack (<20°), the cone-flare produces higher drag coefficients than the delta wing because of its larger frontal area exposed to the flow. In this regime, the delta wing exhibits a weak L/D ratio, as the incoming stream remains nearly parallel to its undersurface, preventing the onset of compression lift. Braking is dominated by drag, but lift generation and hence manoeuvrability remains limited. At higher AoA (20°–40°), the behaviour shifts. The delta wing takes advantage of compression lift by using its shock waves as lifting surfaces [35].

At an angle of attack of 30°, it achieves a drag coefficient of approximately 0.36, compared with 0.22 for the cone-flare (see Table VI), while also enhancing lift performance. As a representative case, the delta wing provides a 63% improvement in L/D relative to the cone-flare, confirming that lifting geometries not only dissipate energy more effectively but also enhance trajectory control by generating useful lift. The underlying mechanism lies in the redistribution of aerodynamic loads: instead of relying solely on drag, as in the cone-flare, the delta wing converts part of the compression-induced pressure field into lift, achieving a more balanced and efficient braking strategy.

To summarize the previous validation results, Table V presents both quantitative and qualitative comparisons between the present study and the available literature. the close agreement obtained for thermal parameters and flow structures supports the reliability and credibility of the adopted CFD methodology.

From a design standpoint, the cone-flare with its higher Aerodynamic mass ratio is best suited for steep, uncontrolled re-entries, favouring rapid energy dissipation but suffering from higher heating and poor manoeuvrability. The delta wing, by contrast, offers a controlled braking regime, spreading heating loads, improving L/D at high AoA, and ensuring smoother trajectory shaping features that align with the objective of optimising lifting re-entry configurations under hypersonic nonequilibrium conditions.

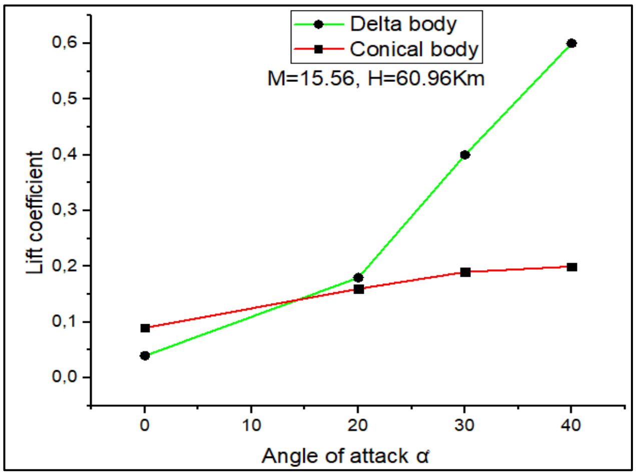

(a)

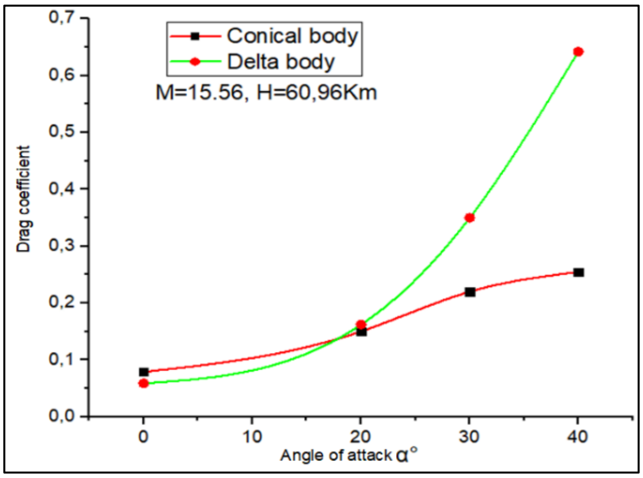

(b)

Fig. 14. Variation of the (a) drag coefficient; (b) lift coefficient with angle of attack.

TABLE VI. Effect of Vehicle Shape on Aerodynamic Braking

Vehicle shape	Delta	Cone flare
Drag coefficient	0.36	0.22
Lift coefficient	0.462	0.173
Aerodynamic mass ratio	$1.753\ 10^{-5}$	$1.869\ 10^{-4}$
L/D	1.28	0.785

B. Influence of Chemical Reaction Models on Wall Temperature and Heat Transfer

Figs. 15 and 16 highlight the strong impact of chemical nonequilibrium models on wall temperature predictions during hypersonic re-entry.The calculations were carried out for a reference flight condition defined by $M_\infty = 15.65$, an altitude of 60.96 km, T_∞ = 244.4 K, $\rho_\infty = 2.745\times10^{-4}$ kg·m⁻³, P_∞ = 19.26 Pa, and $\alpha = 0°$. Under these conditions, three approaches were compared:

- Perfect gas model (Fig. 15(a)): neglecting dissociation, peak relaxation-zone temperature rises to ≈12,500 K.

- Five-reaction model (Fig. 15(b)): limited dissociation pathways reduce the maximum to ≈9800 K.
- Seventeen-reaction Park model (Fig. 15(c)), the most physically comprehensive case, treating air as a five-species neutral mixture (O_2, N_2, NO, O, N) with 15 dissociation reactions and two Zeldovich exchange mechanisms [7, 28], as detailed in Table VII. Here, the maximum temperature drops to ≈8600 K, representing a 28% reduction compared to the perfect gas case.

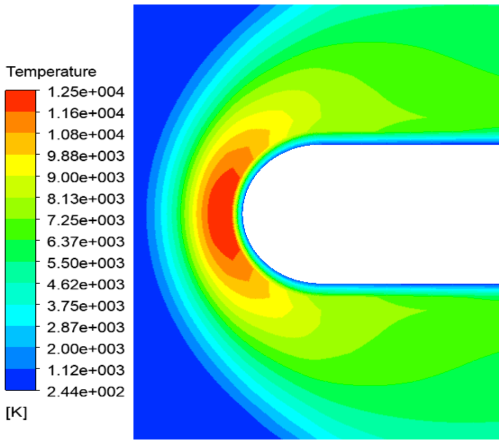

(a)

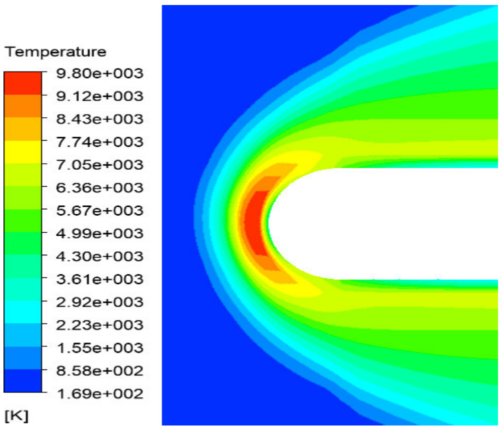

(b)

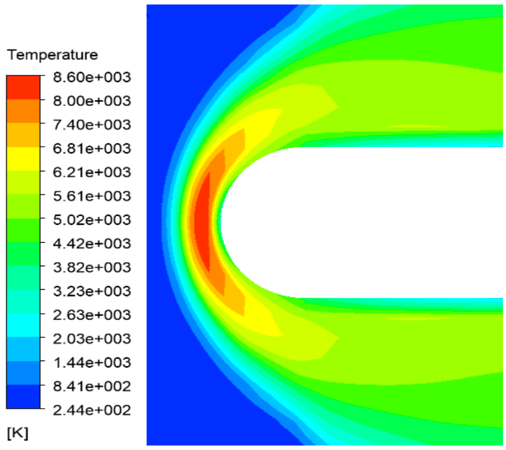

(c)

Fig. 15. Temperature field along surface streamline (a) for Perfect gas; (b) for 5 reactions mechanism; (c) for 17 reactions mechanism.

This systematic reduction underscores the critical role of thermochemical nonequilibrium effects in shaping the thermal environment of re-entry vehicles. In hypersonic flows, the post-shock layer is dominated by vibrational excitation and dissociation of O_2 and N_2. As molecules dissociate, they absorb a significant fraction of the shock energy, which otherwise would contribute directly to translational temperature rise.

This endothermic buffering effect lowers the effective equilibrium temperature, delaying thermal saturation at the vehicle wall. The Zeldovich exchange mechanism further redistributes energy through NO formation, modifying the chemical composition of the boundary layer and reducing peak thermal loads. Collectively, these effects demonstrate why perfect gas assumptions dramatically overpredict heating levels, leading to misleading TPS requirements and excessive structural margins.

TABLE VII. THERMOCHEMICAL MODEL

Reaction		Pre-exponential Factor [$m^3 \cdot mol^{-1} \cdot s^{-1}$]	Activation energy [J/kmol]	Temperature exponent [k]
Dissociation Reaction	$O_2 + M \rightleftharpoons 2O + M$	$1\times10^{+19}$	$4.947\times10^{+08}$	−1.5
	$N_2 + M \rightleftharpoons 2N + M$	$3\times10^{+19}$	$9.412\times10^{+08}$	−1.6
	$NO + M \rightleftharpoons O + N + M$	$1.1\times10^{+14}$	$6.277\times10^{+08}$	0
Recombination Reaction	$N_2 + O \rightleftharpoons NO + N$	$1.8\times10^{+11}$	$3.193\times10^{+08}$	0
	$NO + O \rightleftharpoons N + O_2$	$2.4\times10^{+05}$	$1.598\times10^{+08}$	1

Note: M is a third body (collision partner) acting as a catalyst to remove excess energy. $M \in \{O, N, NO, O_2, N_2\}$.

Fig. 16 further quantifies this trend by showing the wall temperature distribution along the surface streamline. In the stagnation region, the 17-reaction case predicts a maximum wall temperature of nearly 2000 K lower than both the 5-reaction and perfect gas cases. This reduction is critical for re-entry vehicle design, as it directly translates into lighter Thermal Protection System (TPS) requirements.

However, this beneficial reduction comes with a trade-off: as seen in Fig. 15, the lower wall temperature increases the temperature gradient at the wall. According to Fourier's law, this steepened gradient enhances convective heat transfer, especially near the stagnation point where the bow shock directly compresses the gas. Thus, while chemical nonequilibrium lowers the absolute wall temperature, it simultaneously intensifies local convective fluxes in critical fore body regions.

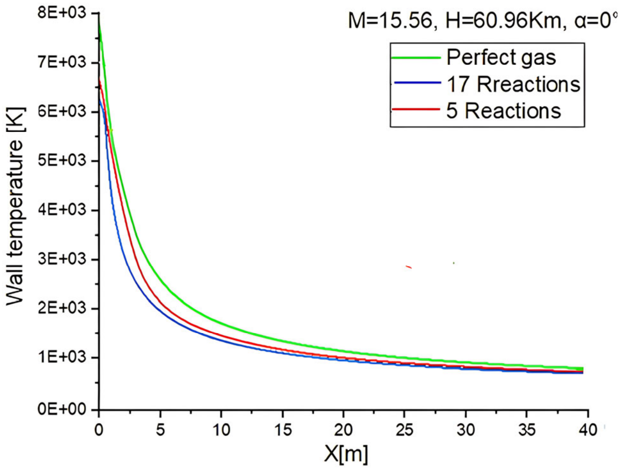

Fig. 16. Wall temperature distribution along surface streamlines.

These findings emphasize three key implications:

(1) Accuracy of thermochemical modelling: Neglecting dissociation by assuming a perfect-gas model leads to an overprediction of wall temperature by approximately 4000 K, resulting in unrealistic Thermal Protection System (TPS) design margins.

(2) Dual role of dissociation/recombination: Dissociation buffers thermal rise (endothermic), while recombination enhances wall heat flux (exothermic). Both must be captured to reflect the true aerothermal environment.

(3) Localized thermal challenges: Even with reduced wall temperature globally, the stagnation-point remains a hot spot due to enhanced convective transport, demanding local reinforcement of TPS materials.

The results indicate that both gas-phase chemistry and boundary recession significantly influence wall heat flux and temperature. In particular, incorporating a more comprehensive air-reaction mechanism leads to a marked reduction in wall temperature, as consistently reported in prior experimental, numerical, and modeling studies [6, 11, 36, 37]. These findings confirm the necessity of employing detailed kinetic schemes, such as Park's 17-reaction model, for predictive hypersonic CFD. This is supported by Refs. [5, 26], who demonstrated that simplified models fail to reproduce measured schlieren structures and wall heat fluxes in shock-dominated flows. In the broader scope of this study, coupling these chemical effects with geometric strategies such as nose blunting and spikes (Figs. 5 and 6) provides a holistic approach: dissociation and exchange reactions reduce thermal loads through energy absorption, while geometric modifications redistribute shock structures to further mitigate stagnation heating. Together, these complementary mechanisms establish the scientific foundation for aerothermal optimisation in future lifting and hypersonic re-entry vehicles.

The progressive reduction in both peak temperatures and equivalent radiative heat fluxes demonstrates the significant role of detailed thermochemical nonequilibrium chemistry in mitigating aerothermal loads during hypersonic re-entry.

Although direct comparisons with published heat-flux measurements remain limited due to differences in flight conditions, Mach numbers, vehicle geometries, wall assumptions, and chemical reaction models, the present results are consistent with the general trends reported in the literature [38]. These findings further support the reliability and predictive capability of the adopted CFD methodology. The corresponding temperatures and equivalent radiative heat fluxes are summarized in Table VIII.

TABLE VIII. EFFECT OF CHEMICAL REACTION MODELS ON PREDICTED AEROTHERMAL QUANTITIES FOR THE CONE-FLARE/BLUNT-BODY CONFIGURATIONS

Chemical reaction model	Peak post-shock temperature (K)	Wall temperature (K)	Equivalent radiative heat flux (MW/m²)*	Reduction in heat flux relative to the perfect-gas model
Perfect gas (Fig 15(a))	12,500	7,600	189	—
5-reactions model (Fig 15(b))	9800	7,000	136	28.0 %
Park 17-reaction model (Fig 15(c))	8600	6,800	121	35.9 %

Note: *Equivalent radiative heat flux estimated assuming a black-body wall using the Stefan–Boltzmann law: $q_{rad} = \sigma T_w^4$, where $\sigma = 5.6704\times10^{-8}$ $W{\cdot}m^{-2}\,K^{-4}$ is the Stefan–Boltzmann constant and T_w is the wall temperature.

C. *Impact of Angle of Attack on Aerodynamic Braking*

Fig. 17 illustrates the influence of varying the Angle of Attack (AoA) on drag coefficient and aerodynamic braking, and by extension on the aerothermal environment during re-entry. As the angle of attack varies between 0° and 40°, the drag coefficient (Cd) rises from about 0.20 to 1.40, an 83% increase, which directly amplifies the deceleration forces acting on the vehicle. Enhanced aerodynamic braking modifies the thermal environment: increased drag promotes stronger shock compression, intensifies the pressure field, and redistributes heating along the forebody [10]. At low angles of attack (<20°), braking is dominated by pure drag with little lift contribution, and the lift-to-drag (L/D) ratio remains weak. In this regime, the thermal loads concentrate around the stagnation point, exposing the Thermal Protection System (TPS) to severe localized heating. Conversely, at higher AoA (20°–40°), the onset of compression lift enables lifting bodies, such as the delta wing, to balance drag and lift more effectively.

This not only enhances manoeuvrability but also spreads heating over a larger surface area, reducing stagnation-point overload and leading to a more favorable thermal distribution.

The drag coefficient also decreases rapidly with Mach number, exhibiting a reduction of nearly 89% between Mach 20 and Mach 6 [22, 31]. This reduction reflects the diminished role of strong shock compression at lower hypersonic speeds, resulting in lesss evere heating environments in the later phases of re-entry.

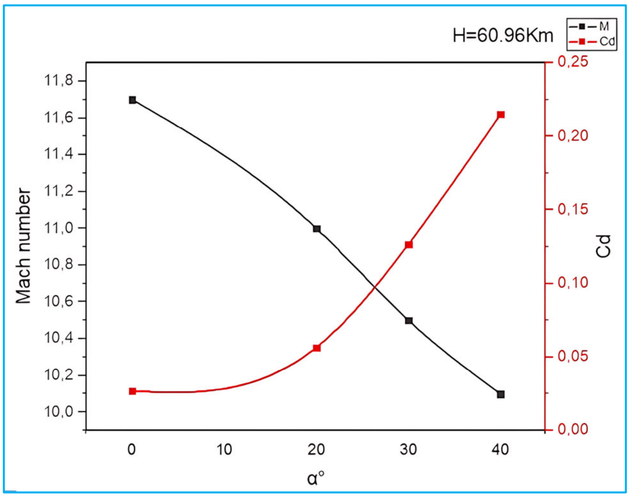

Fig. 17. Variation of drag coefficient and aerodynamic braking with angle of attack for blunt body configuration.

In summary, the angle of attack emerges as a critical parameter for aerothermal prediction, it dictates both the magnitude of aerodynamic braking and the way thermal loads are distributed over the vehicle surface. For lifting configurations such as the delta wing, high AoA operations provide a more advantageous trade-off, combining controlled deceleration with improved thermal management (an essential requirement for the optimization of hypersonic re-entry vehicles under nonequilibrium condition) beyond its aerodynamic effects, the angle of attack also governs the thermal environment along the shock-aligned streamlines.

Fig. 18 compares the surface temperature fields obtained at different angles of attack for the reference atmospheric conditions adopted in this study: Mach 15.65, altitude 60.96 km, $T_\infty = 244.4$ K, $\rho_\infty = 2.745\times10^{-4}$ kg·m^{-3}, and $P_\infty = 19.26$ Pa. The maximum streamline temperature decreases slightly as AoA increases: ≈8600 K at 0°, ≈8415 K at 20°, and ≈8370 K at 40°, corresponding to an overall reduction of about 3%. While this change appears modest, it highlights the effect of dissociation-driven energy absorption at high incidence, where more of the shock energy is redistributed into molecular processes, mitigating the peak thermal load along the streamline. At the same time, AoA alters the shock topology. As the angle increases, the bow shock shifts toward the windward side, which concentrates thermal stresses on this region while shielding the leeward side.

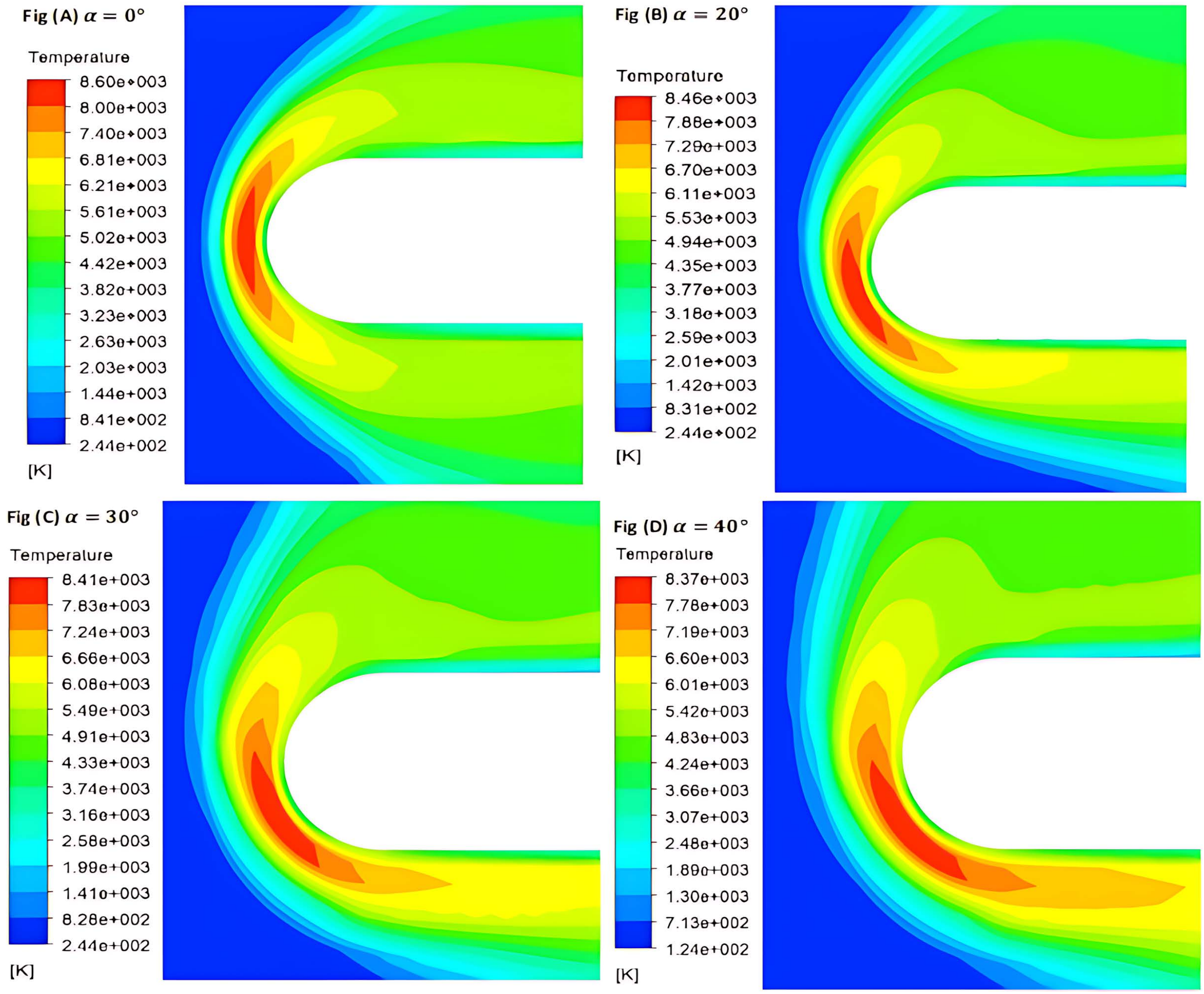

Fig. 18. Streamline surface temperature distributions at different angles of attack for the reference atmospheric condition corresponding to Mach 15.65 and an altitude of 60.96 km ($T_\infty = 244.4$ K, $\rho_\infty = 2.745\times10^{-4}$ kg·m^{-3}, $P_\infty = 19.26$ Pa).

Fig. 19 confirms this redistribution by showing the wall temperature distributions along surface streamlines for different AoA values. At high incidence (e.g., 40°), the difference in temperature between the windward and leeward sides reaches ≈2500 K, a striking asymmetry that spreads the thermal loads across the vehicle instead of concentrating them at the stagnation point. This effect is particularly advantageous for TPS design, as it reduces localized overheating and promotes a more uniform thermal footprint. Taken together, the streamline and wall-temperature analyses demonstrate that higher AoA configurations—although generating stronger drag—provide a dual aerothermal benefit:

(1) A moderate reduction in streamline peak temperatures (≈3%), due to stronger dissociation effects.

(2) A significant redistribution of wall heating (≈2500 K difference windward vs leeward), alleviating stagnation-point overload.

Coupled with the aerodynamic results showing a 63% improvement in L/D at AoA ≈ 30° compared to the cone-flare, these findings emphasise that the delta wing lifting body not only improves trajectory control but also enables more effective thermal management during hypersonic nonequilibrium re-entry. This directly addresses the study's objective of providing validated aerothermal predictions for lifting and hypersonic vehicles under varying geometrical and chemical-kinetic conditions.

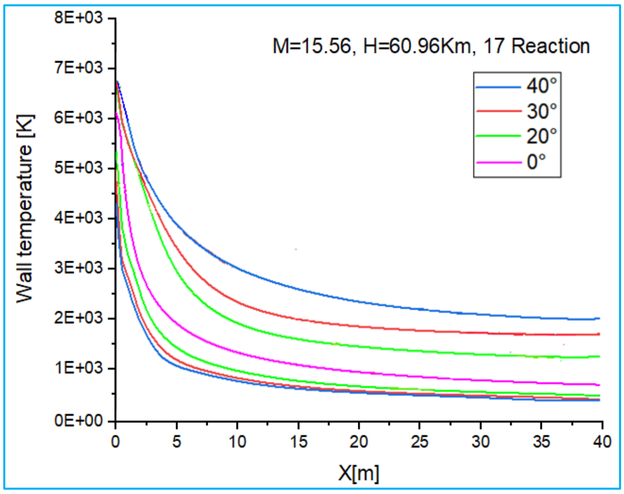

Fig. 19. Influence of the angle of attack on wall temperature along the surface streamlines.

D. Altitude Effect

Re-entry must occur within a narrow trajectory where atmospheric drag is sufficient to slow the vehicle without causing destructive heating. This balance is strongly influenced by altitude, which governs both shock strength and convective heat transfer [2].

Simulations were performed over an altitude range of 60.96–76.20 km, with entry velocities of 4.88–7.32 km/s at a constant AoA = 30°. Results in Fig. 20 show a clear trend: the stagnation-point wall temperature decreases with increasing altitude. At 60 km, the denser atmosphere produces stronger shock compression, yielding the highest surface heating. At 76 km, the reduced density weakens the bow shock, lowering convective transfer and reducing wall temperatures by nearly 15–20% compared to the lower boundary.

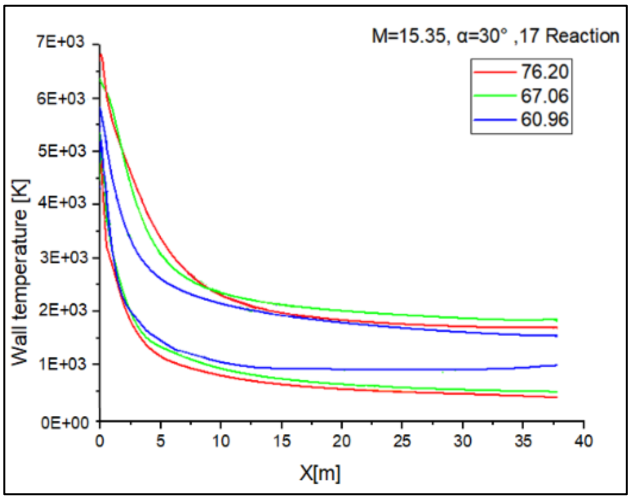

Fig. 20. Wall temperature distribution along surface streamlines for different altitudes.

This behavior reflects the competing roles of density and Mach number. At lower altitudes, high density amplifies stagnation pressure and thermal flux, concentrating heating at the nose region. At higher altitudes, although Mach numbers remain hypersonic, the reduced density dominates, easing the heat load and shifting the heating distribution along the surface. From a predictive standpoint, these results emphasize that altitude is a first-order driver of aerothermal loading. Entering below the safe trajectory leads to excessive drag and heating, risking TPS degradation, while entering too high reduces drag efficiency, risking skip-out. The simulations confirm that accurate altitude-dependent aerothermal prediction is essential to define these overshoot and undershoot boundaries, ensuring reliable trajectory control and thermal safety under nonequilibrium conditions.

E. Blunt Spike Body Effect

During atmospheric re-entry, the nose region of the vehicle experiences severe aerodynamic heating together with intense mechanical stresses, resulting from strong bow shocks and chemically reacting high-enthalpy flows. In this study, a blunt spike was introduced at the vehicle nose to mitigate these loads and improve the survivability of the structure. Wind-tunnel experiments at Mach 6 with a lift-to-drag ratio of 1.0 were validated using Schlieren imaging (Fig. 21(a)) [28] and compared with the present simulations (Fig. 21(b)). The results demonstrate that the spike diffuses the compact bow shock into a conical shape, effectively reducing stagnation-point heating on the nose.

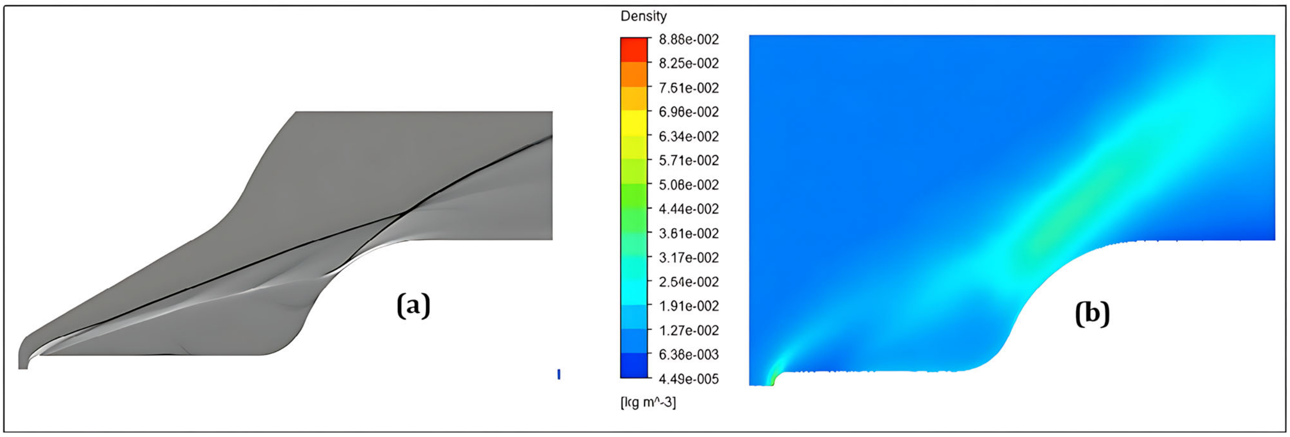

Fig. 21. Comparison of the shock-wave pattern around a blunt body equipped with a spike: (a) Schlieren image from the experiment [28]; (b) numerically predicted Schlieren visualization.

From a thermal perspective, the baseline blunt-nose configuration exhibited a stagnation temperature of approximately 8600 K. With the spike, a local increase in peak temperature up to 9020 K was observed at the spike tip due to its bluntness effect (Fig. 22). However, this localized rise was offset by a significant redistribution of the high-temperature flow.

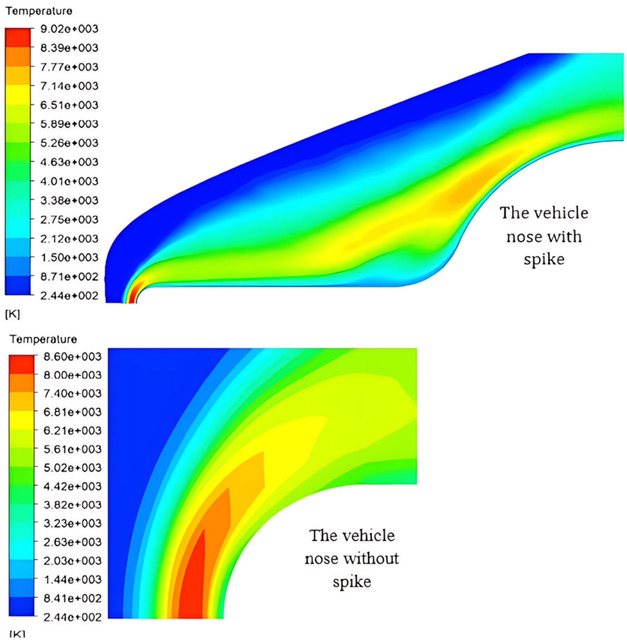

Fig. 22. Thermal contour map of the flow surrounding the spiked blunt body.

The shock was displaced and energy was dissipated along the vehicle shoulder (Fig. 23). Consequently, the effective stagnation temperature at the main nose was reduced to around 7140 K, representing an overall thermal load reduction of about 12.5%. In terms of heat transfer, this improvement can be interpreted using simplified relations: the convective heat flux at the wall is proportional to $q \sim h(T_\infty - T_w)$, where h denotes the convective heat transfer coefficient.

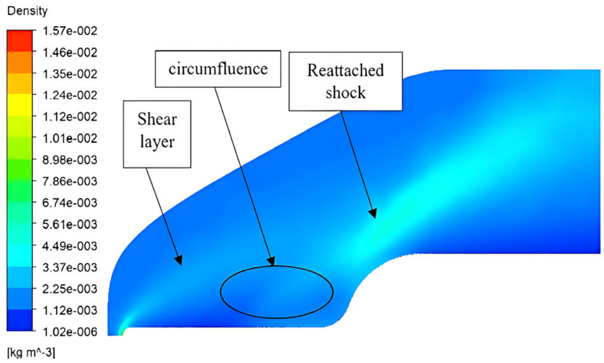

(a)

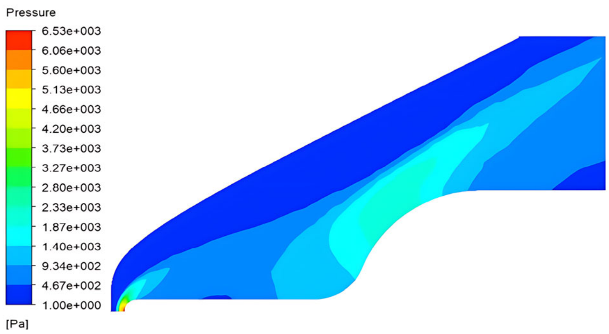

(b)

Fig. 23. Blunt spike (a) density contours; (b) pressure contours.

The introduction of the spike effectively lowers the local heat transfer coefficient by spreading the shock, which corresponds qualitatively to a reduction of the Stanton number and, consequently, a decrease in the Nusselt number at the nose region. In other words, the spike reduces the efficiency with which thermal energy from the flow is transferred to the vehicle's surface.

These combined aerodynamic and thermal benefits highlight the positive role of the blunt spike. Despite the localized heating at its tip, the spike achieves a net reduction in overall thermal stress, enhances the protection of the vehicle's frontal nose, and confirms its suitability as an aerothermal optimization strategy for hypersonic re-entry vehicles.

IV. CONCLUSION

This study investigated the coupled aerothermal and aerodynamic behavior of hypersonic re-entry vehicles, with a specific focus on the interplay between vehicle geometry, chemical reaction modeling, angle of attack, altitude effects, and blunt spike devices. The overall objective was to identify strategies that simultaneously enhance trajectory controllability and reduce thermal loads in realistic nonequilibrium conditions, a challenge that remains central in the development of next-generation re-entry systems.

First, the findings confirm that lifting configurations such as the delta wing significantly outperform axisymmetric bodies, offering a 63% improvement in lift-to-drag ratio while enhancing heat redistribution. In parallel, accurate representation of nonequilibrium chemistry was shown to be indispensable: compared to the perfect gas assumption (≈12,500 K) at Mach = 15.69, the 17-reaction Park model reduced peak relaxation-zone temperatures to ≈8600 K, a 28% decrease driven by dissociation and exchange reactions. Furthermore, variations in angle of attack further optimized performance, with modest reductions in streamline temperatures (≈ 3%) but, more importantly, a 2500 K redistribution of wall heating, alleviating stagnation-point overload and supporting controllability. Similarly, altitude effects proved equally decisive: between 60 and 76 km, reduced density weakened shock strength, lowering wall temperatures by 15–20%. Finally, the blunt spike demonstrated its efficiency as a passive thermal protection device, cutting nose stagnation temperature from ≈ 8600 K to ≈7140 K, a 12.5% reduction, while experimental Schlieren imaging validated the predicted flowfield transformation.

In sum, these results establish a robust and integrated framework for aerothermal optimization. Chemical nonequilibrium processes absorb energy and mitigate heating, while geometric and operational strategies—delta wings, higher AoA, altitude control, and nose spikes redistribute shock structures and thermal fluxes. Their synergistic combination offers a scientifically grounded pathway to the design of future lifting and hypersonic re-entry vehicles, capable of ensuring enhanced safety, controllability, and survivability during hypersonic re-entry.

APPENDIX

Flow Modeling and Governing Equations: The governing flow equations consist of the steady, two-dimensional compressible Navier–Stokes equations (Eqs. (A1)–(A6)). The ideal-gas equation of state was adopted to determine the density, and the dynamic visc osity was obtained from Sutherland's temperature-dependent relation (Eq. (A7)).

A. Species Conservation

For species in a mixture, the mass conservation equation is dictated by:

$$\underbrace{\frac{\partial \rho_\alpha}{\partial t}}_{1}+\underbrace{\frac{\partial}{\partial x}\left(\rho_\alpha u-\left(-q_{\alpha x}^{D}\right)\right)}_{2}+\underbrace{\frac{\partial}{\partial y}\left(\rho_\alpha u-\left(-q_{\alpha y}^{D}\right)\right)}_{3}=\underbrace{\dot{w}_\alpha}_{4} \quad \text{(A1)}$$

The physical significance of the terms in Eq. (A1) is summarized as follows:

Term (1) describes the transient accumulation of species α within the control volume.

Terms (2) and (3) represent the combined convective and diffusive transport of the species in the x and y-directions, respectively.

Term (4) corresponds to the chemical source term, accounting for the local production or consumption of species α. The adopted reaction mechanism satisfies overall mass conservation, such that $\sum_{\alpha=1}^{N_s} \dot{w}_\alpha = 0$ which directly yields the global continuity equation.

Summing Eq. (A1) over all species yields the overall continuity equation: :

$$\underbrace{\frac{\partial \rho}{\partial t}}_{1}+\underbrace{\frac{\partial}{\partial x}(\rho u)}_{2}+\underbrace{\frac{\partial}{\partial y}(\rho v)}_{3}=0 \quad \text{(A2)}$$

In Eq. (A2), Term (1) represents the transient accumulation of the mixture mass, whereas Terms (2) and (3) denote the mass fluxes in the x and y-directions, respectively.

B. Momentum Conservation Equation

The momentum conservation equation for the mixture is expressed as:

$$\underbrace{\frac{\partial \rho u}{\partial t}}_{1}+\underbrace{\frac{\partial}{\partial x}\left(\rho u^2+p-\tau_{xx}\right)}_{2}+\underbrace{\frac{\partial}{\partial y}\left(\rho uv-\tau_{xy}\right)}_{3}=0 \quad \text{(A3)}$$

$$\underbrace{\frac{\partial \rho v}{\partial t}}_{1}+\underbrace{\frac{\partial}{\partial y}\left(\rho v^2+p-\tau_{yy}\right)}_{2}+\underbrace{\frac{\partial}{\partial x}\left(\rho uv-\tau_{xy}\right)}_{3}=0 \quad \text{(A4)}$$

In the above Eqs. (A3) and (A4):

The physical interpretation of Eq. (3) is summarized below:

- Term (1) represents the transient accumulation of the x-momentum.
- Term (2) accounts for momentum transport in the x-direction through convection, pressure, and viscous stresses.
- Term (3) describes the corresponding transport processes in the y-direction.

Eq. (A4) has an analogous interpretation for the remaining momentum component.

C. Vibrational Energy Equation

The vibrational energy equation describes the evolution of the average vibrational energy associated with each molecular species. Its governing form is given by:

$$\underbrace{\frac{\partial}{\partial t}\left(\rho_m e_m^{vib}\right)}_{1}+\underbrace{\frac{\partial}{\partial x}\left(\rho_m e_m^{vib} u-q_{mx}^{vib}\right)}_{2}+\underbrace{\frac{\partial}{\partial y}\left(\rho_m e_m^{vib} v-q_{my}^{vib}\right)}_{3}=\underbrace{\Omega_m}_{4} \quad \text{(A5)}$$

The terms in the vibrational energy equation have the following physical interpretation:

Term (1) represents the transient accumulation of the vibrational energy of species *m*.

Terms (2) and (3) describe vibrational energy transport in the x and y directions, respectively, through convection, diffusion, and thermal conduction.

D. Total Energy Equation

The governing equation for total energy (internal and kinetic) is expressed as:

$$\underbrace{\frac{\partial(\rho E)}{\partial t}}_{1}+\underbrace{\frac{\partial}{\partial x}(\rho E+p)u-(u\tau_{\mathrm{xx}}+v\tau_{\mathrm{Yx}}+qt_{\mathrm{x}})}_{2}+\underbrace{\frac{\partial}{\partial y}((\rho E+p)v-(u\tau_{\mathrm{xx}}+v\tau_{\mathrm{Yx}}+q_{\mathrm{Y}}t))}_{3} \quad \text{(A6)}$$

The physical interpretation of the terms in the total energy equation is summarized as follows:

Term (1) represents the transient accumulation of the total energy within the control volume.

Terms (2) and (3) account for energy transport in the x- and y-directions, respectively. These contributions include convective enthalpy transport, pressure work, viscous work, heat conduction, and enthalpy diffusion.

E. Sutherland's Law

$$\mu=\mu_0\left(\frac{T}{T_0}\right)^{3/2}\frac{(T_0+S)}{(T+S)} \quad \text{(A7)}$$

where μ is the dynamic viscosity, μ_0 is the reference viscosity at T_0, and S denotes Sutherland's constant.

F. Chemical Kinetic Mechanism

A five-species air model (N_2, O_2, NO, N, and O) was adopted to describe the thermochemical nonequilibrium flow. Vibrational equilibrium was assumed, while ionization effects were neglected. The adopted chemical mechanism follows Ref. [5], and the corresponding reactions together with their kinetic parameters are summarized in Table VII.

$$O_2 + O \rightleftharpoons 2O + O \quad \text{(A8)}$$

$$O_2 + N \rightleftharpoons 2O + N \quad \text{(A9)}$$

$$O2 + NO \rightleftharpoons 2O + NO \quad \text{(A10)}$$

$$O_2 + O_2 \rightleftharpoons 2O + O_2 \quad \text{(A11)}$$

$$O_2 + N_2 \rightleftharpoons 2O + N_2 \quad \text{(A12)}$$

$$N_2 + O \rightleftharpoons 2N + O \quad \text{(A13)}$$

$$N_2 + N \rightleftharpoons 2N + N \quad \text{(A14)}$$

$$N_2 + NO \rightleftharpoons 2N + NO \quad \text{(A15)}$$

$$N_2 + O_2 \rightleftharpoons 2N + O_2 \quad \text{(A16)}$$

$$N_2 + N_2 \rightleftharpoons 2N + N_2 \quad \text{(A17)}$$

$$NO + O \rightleftharpoons N + O + O \quad \text{(A18)}$$

$$NO + N \rightleftharpoons N + O + N \quad \text{(A19)}$$

$$NO + NO \rightleftharpoons N + O + NO \quad \text{(A20)}$$

$$NO + O_2 \rightleftharpoons N + O + O_2 \quad \text{(A21)}$$

$$NO + N_2 \rightleftharpoons N + O + N_2 \quad \text{(A22)}$$

$$N_2 + O \rightleftharpoons NO + N \quad \text{(A23)}$$

$$NO + O \rightleftharpoons N + O_2 \quad \text{(A24)}$$

Chemical source terms arise from the elementary reactions occurring among the gas species. The resulting mass production and consumption rates are obtained by summing the contributions of all elementary reactions. Considering the r^{th} reaction within a mechanism of *Nr* elementary reactions involving *Ns* species, the reaction can be written as:

$$\sum v'_{\alpha,r} X_\alpha = \sum v''_{\alpha,r} X_\alpha \quad \text{(A25)}$$

Eq. (A25) represents a reversible elementary reaction, with $\acute{v}_{\alpha,r}$ and $\ddot{v}_{\alpha,r}$ denoting the stoichiometric coefficients of species α in the reactants and products, respectively, and Xα its mole fraction. The forward and reverse reaction rates are evaluated according to Refs. [3, 5]:

Forward reaction:

$$d\left[X_\alpha\right]_r^f/dt=\left(v''_{\alpha,r}-v'_{\alpha,r}\right)\left(k_{f,r}\prod_{\alpha=1}^{N_s}\left[X_\alpha\right]^{v'_{\alpha,r}}\right) \quad \text{(A26)}$$

Backward reaction:

$$d\left[X_\alpha\right]_r^b/dt=\left(v''_{\alpha,r}-v'_{\alpha,r}\right)\left(k_{b,r}\prod_{\alpha=1}^{N_s}\left[X_\alpha\right]^{v''_{\alpha,r}}\right) \quad \text{(A27)}$$

where $K_{f,r}$ and $K_{b,r}$ represent the forward and reverse rate constants of reaction *r*. The forward rate constant is computed in ANSYS Fluent using the Arrhenius law:

$$K_{f,r}=C_{f,r}T_{f,r}^{n_{f,r}}\,e^{\frac{-E_{f,r}}{kT_{f,r}}} \quad \text{(A28)}$$

where:

- $K_{f,r}$: Reaction rate constant for the forward (f) or reverse (r) process.
- $C_{f,r}$: Pre-exponential (frequency) factor, reflecting the frequency of effective molecular collisions in the reaction.
- $T_{f,r}$: Absolute gas temperature associated with the reacting system.
- $n_{f,r}$: Empirical temperature exponent, characterizing the sensitivity of the rate constant to temperature variations beyond simple Arrhenius behavior.
- $E_{f,r}$: activation energy, the minimum energy required for the reaction to occur.
- *k*: Boltzmann constant, relating energy to temperature at the molecular scale.*e*: exponential term

representing the fraction of molecules energetic enough to overcome the activation barrier.

Conflict of Interest

The authors declare no conflict of interest.

Author Contributions

Rachid Renane: Project administration, Conceptualization, Formal analysis, Investigation, Methodology, Software, Supervision, Validation, Visualization, Writing—original draft, Writing—review & editing. Rachid Allouche: Project administration, Conceptualization, Formal analysis, Investigation, Methodology, Supervision, Software, Visualization, Validation. Ahmed Neche: Project administration, Methodology, Formal analysis, Supervision, Validation. Oumaima Zmit: Software, Validation, Visualization, Formal analysis, Writing—review & editing. All authors had approved the final version.

Acknowledgment

The authors would like to thank the Laboratory of Aeronautical Sciences at the University of Blida 1 for providing the computational resources and high-performance computing facilities used throughout this project.

References

[1] R. Allouche, R. Renane, and R. Haoui, "Prediction of the optimal speed of an aerospace vehicle by aerothermochemical analysis of hypersonic flow during atmospheric re-entry," *Mech. Ind.*, vol. 21, 208, 2020. doi: 10.1051/meca/2020006

[2] J. M. Wallace and P. V. Hobbs, *Atmospheric Science: An Introductory Survey*, San Diego, CA, USA: Academic Press, 2006.

[3] R. Allouche, R. Haoui, and R. Renane, "Numerical simulation of reactive flow in non-equilibrium behind a strong shock wave during re-entry into Earth's atmosphere," *Mech. Ind.*, vol. 15, pp. 81–87, 2014. doi: 10.1051/meca/2014002

[4] D. Dirkx and E. Mooij, "Optimization of entry-vehicle shapes during conceptual design," *Acta Astronaut.*, vol. 92, no. 2, pp. 169–180, 2013. doi: 10.1016/j.actaastro.2013.08.006

[5] Z. Tang, H. Xu, X. Li, and J. Ren, "Aerodynamic heating in hypersonic shock wave and turbulent boundary layer interaction," *J. Fluid Mech.*, vol. 999, A66, 2024. doi: 10.1017/jfm.2024.641

[6] M. Auweter-Kurtz *et al.*, "Characterization of high enthalpy flows," in *High Enthalpy Flow Diagnostics*, Stuttgart, Germany: Univ. Stuttgart, Inst. Space Syst., 2005, pp. 199–220.

[7] R. Allouche, "Numerical simulation of radiation effects on thermochemical parameters behind a shock wave," Ph.D. Dissertation, USTHB, Algiers, Algeria, 2014. (in French)

[8] M. Leonurd, L. Weinstein, and L. Neul, "Hypersonic performance of several basic and modified diamond-cross-section delta-wing configurations," NASA, Washington, D.C., USA, Tech. Note NASA TN D-4091, 1967.

[9] T. Soubrie, "Accounting for ionization and radiation in the modeling of Earth and Mars atmospheric entry flows," Ph.D. Dissertation, ISAE-SUPAERO, Toulouse, France, 2006. (in French)

[10] H. Guilai and Z. Jiang, "Hypersonic flow field reconfiguration and drag reduction of blunt body with spikes and sideward jets," *Int. J. Aerosp. Eng.*, vol. 2018, 7432961, 2018. doi: 10.1155/2018/7432961

[11] C. Park, J. T. Howe, R. L. Jaffe, and G. V. Candler, "Review of chemical-kinetic problems of future NASA missions: Mars entries," *J. Thermophys. Heat Transf.*, vol. 8, no. 1, pp. 9–23, 1994.

[12] L. H. Townend, "Research and design for lifting reentry," *Prog. Aerosp. Sci.*, vol. 19, pp. 1–80, 1979. doi: 10.1016/0376-0421(79)90001-0

[13] A. Singh, "Flow over a delta wing and blunt body combination at hypersonic speeds," in *Proc. 19th ICAS Congr.*, 1994, pp. 356–361.

[14] F. Deng, Z. Jiao, B. Liang, F. Xie, and N. Qin, "Spike effects on drag reduction for hypersonic lifting body," *J. Spacecr. Rockets*, vol. 54, no. 6, pp. 1417–1428, Nov.–Dec. 2017. doi: 10.2514/1.A33865

[15] N. E. Afonina, A. Y. Vlasov, and V. G. Gromov, "Numerical analysis of heat transfer on the surface of a delta wing in a hypersonic air flow at large angle of attack," *Fluid Dyn.*, vol. 19, pp. 845–848, 1984. doi: 10.1007/BF01093561

[16] D. M. Rao, "Hypersonic aerodynamic characteristics of flat delta and caret wing models at high incidence angles," *J. Spacecr. Rockets*, vol. 7, no. 12, pp. 1475–1476, 1970. doi: 10.2514/3.30197

[17] S. Yang, I. Choi, and G. Park, "Development of combined hypersonic test facility for aerothermodynamic testing," *PLOS ONE*, vol. 19, no. 2, e0298113, 2024. doi: 10.1371/journal.pone.0298113

[18] H. Rahman, S. Khushnood, A. Raza, and K. Ahmad, "Experimental and computational investigation of delta wing aerodynamics," in *Proc. IBCAST 2013*, 2013, pp. 1–6. doi: 10.1109/IBCAST.2013.6512155

[19] V. Shanbhag, "Numerical studies on hypersonic delta wings with detached shock waves," Aeronaut. Res. Council, Rep. ARC-1974, 1974.

[20] H. Qiu, M. Shi, Y. Zhu, and C. Lee, "Boundary layer transition of hypersonic flow over a delta wing," *J. Fluid Mech.*, vol. 980, A57, 2024. doi: 10.1017/jfm.2024.42

[21] Y. Xi, B. Yan, G. Yang, X. Sha, D. Zhu, and S. Fu, "Numerical simulations of attachment-line boundary layer in hypersonic flow, Part I: Roughness-induced subcritical transitions," *J. Fluid Mech.*, vol. 1012, A15, 2025. doi: 10.1017/jfm.2025.269

[22] W. Zhang, Z. Zhang, X. Wang, and T. Su, "A review of the mathematical modeling of equilibrium and nonequilibrium hypersonic flows," *Adv. Aerodyn.*, vol. 4, 38, 2022. doi: 10.1186/s42774-022-00125-x

[23] P. M. Seltner, S. Willems, and A. Gülhan, "Aerodynamic interactions of blunt bodies free-flying in hypersonic flow," *Exp. Fluids*, vol. 65, 80, 2024. doi: 10.1007/s00348-024-03818-9

[24] J. Kim, J. Nam, J. Hur, J. Kim, and B. J. Lee, "Experimental study of nose-tip bluntness effects on hypersonic boundary-layer transition in a shock tunnel," *Sci. Rep.*, vol. 15, 38301, 2025. doi: 10.1038/s41598-025-22323-5

[25] J. L. Everhart and F. A. Greene, "Turbulent supersonic/hypersonic heating correlations for open and closed cavities," in *Proc. AIAA Conf.*, 2009, pp. 2009–1400. doi: 10.2514/6.2009-1400

[26] C. Gonzalez, J. Castillo, and A. Shirin, "Hypersonic heat flux prediction and validation," in *Proc. AIAA SciTech 2025 Forum*, 2025, pp. 2025–2634. doi: 10.2514/6.2025-2634

[27] I. T. Karpuzcu and D. A. Levin, "Loss of axial symmetry in hypersonic flows over conical shapes," *Phys. Rev. Fluids*, vol. 10, no. 3, 033901, 2025. doi: 10.1103/PhysRevFluids.10.033901

[28] R. Guzmán-Bohórquez, P. C. Greco Júnior, and H. D. Cerón-Muñoz, "Aerodynamic analysis applied to a hypersonic vehicle type waverider through CFD," in *Proc. COBEM 2023*, 2023. doi: 10.26678/abcm.cobem2023.cob2023-2028

[29] F. F. J. Schrijer, F. Scarano, and B. W. van Oudheusden, "Experiments on hypersonic boundary layer separation and reattachment on a blunted cone-flare using quantitative infrared thermography," in *Proc. AIAA Int. Space Planes Hypersonic Syst. Technol. Conf.*, 2003, pp. 2003–6967. doi: 10.2514/6.2003-6967

[30] H. Panjagala, "Aerothermodynamics topology optimization of hypersonic re-entry vehicle with aerospike using CFD," *Int. J. Mech. Eng. Technol.*, vol. 9, no. 1, pp. 1114–1123, 2018.

[31] A. Boulahiya, "Hypersonic boundary layer in viscous flows with chemical non-equilibrium," Ph.D. Dissertation, Univ. Mentouri, Constantine, Algeria, 2010. (in French)

[32] N. Ghendour, S. Ouchene, R. Allouche, and R. Renane, "Numerical simulation of a hypersonic flow around a blunt body of space shuttle nose type," *Sci. Technol. B (Univ. of Constantine, Algeria)*, no. 43, pp. 35–41, Jun. 2016.

[33] A. Lordi, R. J. Vidal, and C. B. Johnson, "Chemical nonequilibrium effects on simplified shuttle configurations," NASA Langley Res. Center, Hampton, VA, USA, Tech. Rep., 1973.

[34] H. Ottens, “Preliminary computational investigation on aerodynamic phenomena on Delft Aerospace Re-entry Test Vehicle (DART),” in *Proc. 4th Symp. Aerothermodyn. Space Veh.*, 2002.
[35] J. D. Anderson, *Compressible Fluid Flow*, 4th ed. New York, NY, USA: McGraw-Hill Education, 2020.
[36] Z. Mei, “Coupled simulation for reentry ablative behavior of hypersonic vehicles,” *IOP Conf. Ser. Mater. Sci. Eng.*, vol. 892, 012028, 2020. doi: 10.1088/1757-899X/892/1/012028
[37] M. E. Holloway, “Detailed analysis of thermochemistry modeling for hypersonic air flows,” Ph.D. Dissertation, Univ. Michigan, Ann Arbor, MI, USA, 2021.
[38] P. Liao, W. Song, P. Du, and F. Feng, “Aerodynamic interference reduction using aerospike for two-stage reusable launch vehicle,” *J. Aerosp. Eng.*, vol. 36, no. 4, 06023002, 2023. doi: 10.1061/JAEEEZ.ASENG-4668